

# Propulsive jet influence on generic launcher base flow

S. Stephan<sup>1</sup> · J. Wu<sup>1</sup> · R. Radespiel<sup>1</sup>

Received: 20 January 2015 / Revised: 4 May 2015 / Accepted: 26 May 2015 / Published online: 29 June 2015  
© CEAS 2015

**Abstract** Afterbody flow phenomena represent a significant source of uncertainties in the design of a launcher. Therefore, there is a demand for measuring such flows in wind tunnels. For propulsive jet simulation a new jet facility was integrated into a hypersonic/supersonic wind tunnel. The jet simulation resembles the generic model of a staged rocket launcher. The design and the qualification of the facility are reported. This includes measurements of pressure, temperature and Mach number distribution. Pressure and Schlieren measurements are conducted in the wake of the generic launcher. The unsteady pressure characteristics at the generic rocket base and fairing are analyzed for supersonic and hypersonic freestream. The influence of the under-expanded jet is reported and the jet temperatures are varied. On the base fluctuations at a Strouhal number around 0.25 dominates supersonic freestream flows. Additionally, a fluctuation level increase on the base is observed for Strouhal numbers above 0.75 in hypersonic flow regime, which is attributed to the interactions of wake flow and jet.

**Keywords** Jet simulation · Base flow · Afterbody flow · Generic rocket · Launcher · Unsteady pressure fluctuations

## 1 Introduction

The interest in jet simulation is motivated by the need for experimental data in the area of afterbody flow phenomena. During atmospheric rocket flight, a multitude of interactions between freestream and jet are developed. The area of interest is the wake flow of the generic rocket model. The wake flow is characterized by a strongly oscillating flow (buffet) due to the interactions of the turbulent base flow shear layer and its reattachment on the nozzle fairing with the external flow and the dynamics of the propulsive jet. These interactions can lead to significant wall pressure oscillations and therefore dynamic loads. Moreover, the locally reverse flow to the base can bring about base flow heating augmentation. While the highest mechanical dynamic loads are generally expected at transonic trajectory points, understanding base flow sensitivities at higher speeds is important, as the formation of expansion waves and shocks changes with freestream Mach number and the displacement effect of the under-expanded propulsive jet changes as well. A number of experimental and numerical investigations are reported in the literature on missiles with blunt bases [1–5, 7–9, 12, 14–16, 18, 23] and boat-tailed bases [1, 7, 9, 13, 18, 20–22]. Most investigations are done in transonic and low supersonic flow regimes without jet. Generic launcher models consisting of two cylindrical bodies (large main body and nozzle fairing), as used here, are reported by [6, 10, 11, 15, 19, 25–28]. Scaled Ariane 5 models are investigated by [17, 24, 26, 43, 44]. Most research is conducted without jet flow. Jet effects on the base are presented by several authors [1, 6, 13, 15, 18, 20].

Peters [21, 22] researched the effect of the boattail drag for different jet simulation parameters by variation of the boattail, the nozzle exit to throat ratio, the jet temperature

---

✉ S. Stephan  
s.stephan@tu-bs.de

<sup>1</sup> Institute of Fluid Mechanics, Technische Universität Braunschweig, Hermann-Blenk-Str. 37, 38108 Braunschweig, Germany

and the gas composition. Kumar [23] presented investigations in boattail separated flows relevant to launch vehicle configurations. This included mean and fluctuation pressure measurements. The investigations were made at transonic speeds ranging from  $M = 0.7$ – $1.2$  and for various boattail angles and diameter ratios. Investigations of the Ariane 5 European launcher afterbody at a scale of 0.01 have been conducted by Reijasse [24]. The main stage including the main stage engine and boosters was studied in a blow-down wind tunnel at  $M = 4$ . The jet was simulated with cold high-pressure air, which was expanded to resemble flight at an altitude of 30 km. As a result the complex flow field consisting of supersonic, subsonic and reverse flows was determined. Pain et al. [43] performed numerical investigations at generic launcher consisting of a generic launcher model (central body) and two additional side cylinders similar to the Ariane 5 launcher boosters at the freestream Mach number 0.702. They found significant discrepancies in the instantaneous, statistical and fluctuation flow features with and without booster. It turns out that axisymmetric body experiments are usually not representative for a configuration with boosters. Schwane [44] discusses efficient methods for spacecraft design and optimization using numerical and experimental flow and structure data from Ariane 5 and Vega experiments. Schwane showed that these complex unsteady flow topologies have to be monitored carefully relating to data post-processing, filtering and statistical convergence. Deck et al. [6] and Deprés [15] investigated a generic rocket model at transonic speed with an over-expanded jet. Both found that the wake flow is dominated by coherent antisymmetric modes at the flapping and vortex shedding frequencies, whereas the effect of the over-expanded jet is rather small. Numerical research on a two-dimensional and an axisymmetric afterbody at transonic speed are done by Weiss et al. [10, 19]. The computations show a global motion for the two-dimensional wake flow and a more complex turbulence mechanism with several modes for the axisymmetric flow. Bitter et al. [11] did high-repetition-rate PIV measurements for boundary layer and wake flow investigations on a generic rocket model. They measured the characterization of shedding vortices in the wake and Reynold stresses in the shear layer in a Mach number range from 0.3 to 2.6. Further a temporal analysis of the wake spectrum is presented with the result that the vortex shedding is not periodical. Published base flow characteristics at higher speeds are sparse. Saile et al. [27, 28] investigated afterbody pressure fluctuations at  $M = 6$  and researched different fairing extensions and plume effects. They analyzed base pressure fluctuations and found global modes for flapping and shedding. The results with jet shows additional high frequencies information. Statnikov et al. [25, 26] performed numerical flow analysis of the wake of a generic launcher model at  $M = 6$  including

dynamic mode decomposition analysis. Using this analysis they associated dominating frequencies to wake flow phenomena, i.e., longitudinal pumping of the cavity, a swinging mode of the shear layer and a radial flapping motion of the shear layer.

In this paper, a new jet simulation facility for cost-effective research on turbulent afterbody flows is presented. Some characteristic jet properties such as velocity ratio can be adjusted to match real flight conditions. The jet simulation facility in its current stage can be run in stagnant air and also with high-speed outer flow. The jet simulation facility is of the Ludwig tube blow-down type. The Ludwig tube works with a fast-acting valve and a good flow quality is obtained at low operational cost. Detailed information about Ludwig tubes with fast-acting valves are presented by Koppenwallner [29]. Usually, Ludwig tubes are cold blow-down facilities. In the present case the storage tube used for jet simulation can be heated up to 900 K and gas of low molar mass can be employed to adjust characteristic jet properties. The new jet simulation facility is integrated into a large outer Ludwig tube that generates the high-speed flow field around the afterbody. The overall wind tunnel configuration is rather simple and it allows for cost-efficient and high-quality research which can be afforded by university laboratories. The jet simulation facility is used for investigations of the turbulent wake of a generic space launcher. For different freestream Mach numbers the jet temperature influence of the base flow is analyzed.

## 2 Design approach of jet simulation

For simulating rocket afterbody flows in wind tunnel facilities, it is important to reproduce sensitivities of rocket plume flow parameters. A review of various techniques for simulation of jet exhaust in ground testing facilities is given by Pindzola [30]. The scaling of the rocket plume for the jet simulation facility used in the present work is based on recent European research projects in rocket propulsion [31]. The launcher chosen to be scaled is the Ariane 5 with a Vulcain 2 rocket motor at an altitude of 50.9 km. The presented design is hence for hypersonic flight as displayed in Table 1. The variations of freestream and nozzle parameters at two trajectory points for flight and in the wind tunnel are given in Table 2. The trajectory data are taken from the launch kit flight 202 Ariane 5 [37].

The most obvious approach would be a geometric scaling; for wind tunnel testing that is a very difficult approach. Rocket motors used in launchers have hot rocket plumes with total temperatures in excess of 3000 K. This high temperature would create extreme heat loads on the wind tunnel models, limit the use of sensors, and the infrastructure

cost are extremely high. Hence jet simulations in wind tunnels usually employ cold plumes. But for physics-based ground simulation, two major afterbody flow mechanisms are important and should be considered. One mechanism is flow displacement by plume shape. The plume shape affects the positions of the shear layer and the plume shock. It mainly depends on the ratio of nozzle exit pressure to static pressure in the freestream. The second mechanism is flow entrainment into the plume. The entrainment describes the effect of the shear layer to entrain gas from the base flow.

Entrainment results from turbulent mixing and this is associated with large turbulent structures in the afterbody flow. Simulation of turbulent mixing is therefore needed to represent buffet flow phenomena at the rocket afterbody. The differences between wind tunnel and rocket operation plume conditions affect the similarity parameters for entrainment such as the velocity ratio. The low

total temperature used in wind tunnel facilities reduces the exhaust velocity. Varying the specific heat ratio of the plume fluid affects the exit Mach number and the flow expansion. The exhaust velocity is also affected by different gas molar masses. Finally, a higher density of the jet flow will affect the shear layer growth. In conclusion, entrainment and growth of mixing layers are governed by two important parameters. The first is the freestream velocity to plume velocity ratio,  $(u_p - u_\infty)/u_p$ . This parameter is expected to govern turbulence production in the shear layer and unsteadiness of the afterbody flow. The second parameter is the momentum ratio  $(\rho_p u_p)/(\rho_\infty u_\infty)$ . This parameter will affect the growth of the shear layer and its position relative to the nozzle axis. Note that the plume velocity is not equal to the nozzle exit velocity. Rather, the plume velocity is the velocity in the region between the shear layer and the barrel shock of the under-expanded jet, see Fig. 1. The velocity ratio and the momentum ratio should be varied in significant amounts by using the facility to make experiments representative. For assessing the potential

**Table 1** The jet simulation parameters for the facility (air and helium) and for the rocket motor Vulcain 2

	Working gas air	Working gas He	Vulcain 2
$p_{t, \text{reservoir}}$ , bar	20	19	116
$T_{t,e}$ , K	620	620	3630
$M_e$	2.5	2.5	4.56
$p_e/p_\infty$	93	90	180
$p/p_\infty$	1582	1503	152,833
$u_e/u_\infty$	0.9	2.3	2.6
$(u_{\text{max}} - u_\infty)/u_{\text{max}}$	0.19	0.65	0.69
$T_e/T_\infty$	4.7	3.5	5.4
$\rho_e/\rho_\infty$	19.5	3.6	15.5
$\rho_e u_e/\rho_\infty u_\infty$	18	8	41
$\rho_e u_{\text{max}}/\rho_\infty u_{\text{max}}$	24	10	49
$\rho_e u_e^2/\rho_\infty u_\infty^2$	17	19	106
$e_{t,e}/e_{t,\infty}$	1.3	6.9	8.7

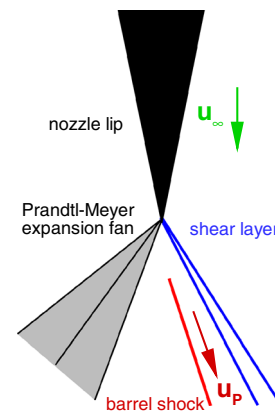


**Fig. 1** Sketch of the flow at the nozzle lip

**Table 2** Freestream and jet simulation parameters for the supersonic and hypersonic configuration

	Supersonic configuration		Hypersonic configuration	
	Wind tunnel/jet simulation	Ariane 5/vulcain 2	Wind tunnel/jet simulation	Ariane 5/vulcain 2
$p_\infty$ , bar	$4.1 \times 10^{-2}$	$2.7 \times 10^{-2}$	$1.2 \times 10^{-2}$	$7.6 \times 10^{-4}$
$T_\infty$ , K	102	217	58	217
$M_\infty$	2.9	3	5.9	5.5
$Re_D$	$1.3 \times 10^6$	$1.4 \times 10^7$	$1.8 \times 10^6$	$7.6 \times 10^5$
$p_{t, \text{reservoir}}$ , bar	4.1	116	20.4/18.8/17.5	116
$T_{t,e}$ , bar	280/470/620	3630	280/470/620	3630
$p_e/p_\infty$	5.7	5.7	94.5/87.1/81	180
$(u_{\text{max}} - u_\infty)/u_{\text{max}}$	0.20/0.38/0.46	0.83	-0.19/0.07/0.19	0.66
$(u_{\text{max}} - u_\infty)/u_{\text{max}}$ (He)	0.64/0.73/0.76		0.48/0.59/0.65	

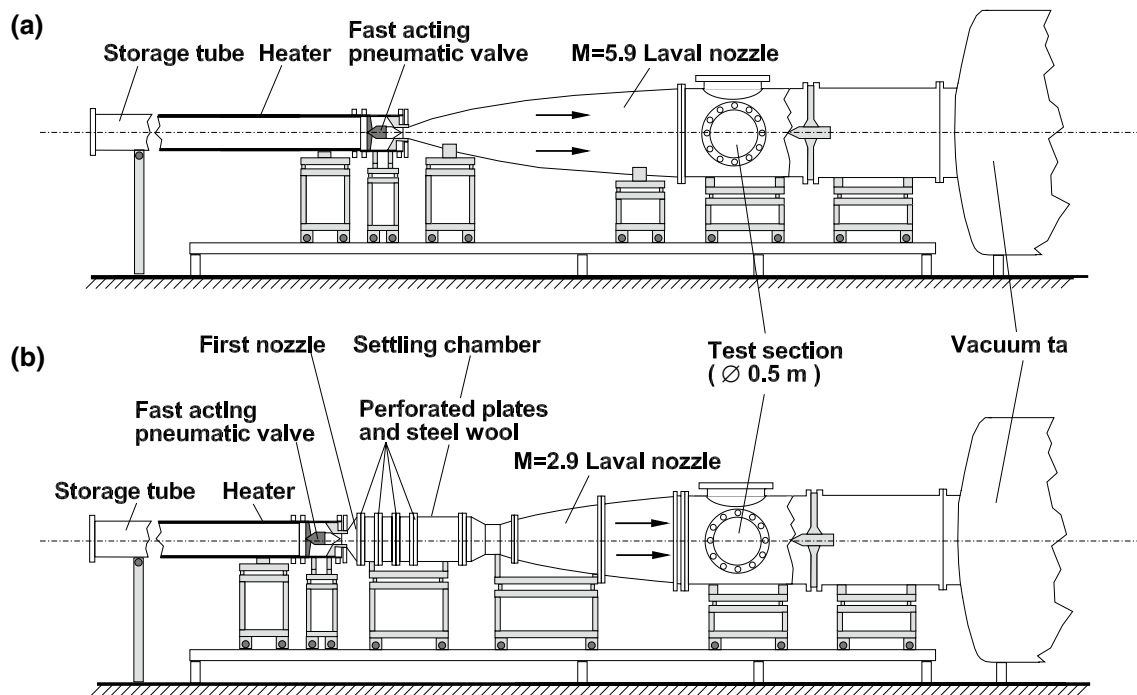


**Fig. 2** Sketch of the Hypersonic Ludwig Tube Braunschweig. *Top* hypersonic configuration, *bottom* supersonic configuration

of the wind tunnel setup, a simple estimate is to observe the plume velocity for expansions to  $p = 0$ . In this case the plume velocity  $u_p$  is replaced by  $u_{\max} = [(2\kappa)/(\kappa - 1)] (\mathfrak{R}T_t/M_{\text{Mol}})^{-1/2}$ . This formula shows that the maximum velocity depends on the molar mass  $M_{\text{Mol}}$ , the gas constant  $\mathfrak{R}$ , the specific heat ratio  $\kappa$  and the total temperature  $T_t$ . Therefore, by changing the gas composition the velocity can be modified. Note that the error using the maximum velocity compared to realistic plume velocities is around 7–8 %. The maximum velocity for the Vulcain 2 ( $\text{H}_2/\text{O}_2$  combustion;  $\kappa = 1.2$ ;  $M_{\text{Mol}} = 13.5$  g/mol) is  $u_{\max, \text{Vulcain 2}} = 5172$  m/s at  $T_t = 3630$  K. Heated air ( $\kappa = 1.4$ ;  $M_{\text{Mol}} = 29$  g/mol) reaches 25 % and heated helium ( $\kappa = 1.67$ ;  $M_{\text{Mol}} = 4$  g/mol) 56 % of  $u_{\max, \text{Vulcain 2}}$  at  $T_t = 800$  K. Note that chemical effects in the jet may not be well represented by using gases with different specific heat ratio and different molar mass. In Table 1 important parameters for jet simulation for the Vulcain 2 and for the jet simulation facility with different working gases are presented. These data are calculated using one-dimensional compressible flow theory and therefore the given values are assumed to be constant across the jet exit plane. The exit pressure in real truncated nozzles varies significantly across the exit plane. Typically, the pressure at the axis is 20 % lower compared to the one-dimensional value, and its value at the lip is 10 % higher, according to our experience from numerical flow simulations with heated air jets. A number

of 20 % may therefore be regarded as another systematic error of the present one-dimensional analysis. The first parameter, nozzle to freestream pressure ratio  $p_e/p_\infty$ , shows the degree of under-expansion. The Vulcain 2 expansion is twice as large as in the present simulation facility. The second ratio is the total nozzle to freestream pressure ratio  $p_t/p_\infty$ . This ratio is inherently much smaller in a wind tunnel facility without a high-pressure feeding system of the flow in the combustion chamber. The nozzle exit velocity to freestream velocity ratio  $u_e/u_\infty$  is much too small compared to Vulcain 2 if air is used as a jet fluid. When helium is used as working gas the velocity ratios are quite similar. Also full simulation capability of the  $(u_{\max} - u_\infty)/u_{\max}$  ratio and the nozzle exit to freestream temperature ratio is achieved. Note that the nozzle exit Mach number is significantly below the Vulcain 2 value. As this Mach number affects the nozzle exit flow parameters pressure, density, temperature and velocity, it can be adjusted to improve the jet simulation parameters given in Table 1. For example, using the original exit Mach number of 4.56 would result in a pressure ratio,  $p_e/p_\infty = 5$  for the working gas of air, which is much too low in order to represent the plume shape. Similar effects are observed for the parameters related to temperature, density and momentum. The lower exit Mach number appears to represent a good compromise for jet simulation. Nevertheless, the density and the momentum ratios exhibit some differences for both working gases as

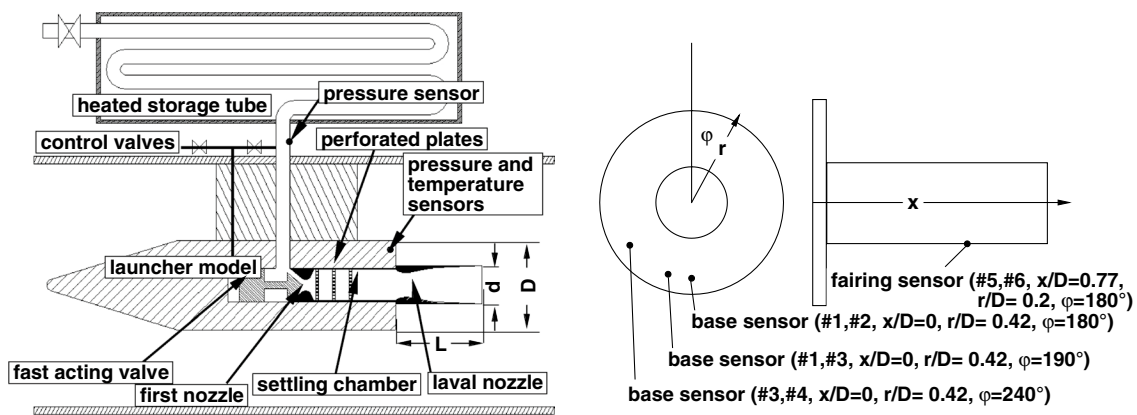


**Fig. 3** Sketch of the jet simulation facility (right). Kulite sensor positions (left). The nozzle diameter is  $d = 43$  mm and the nozzle length is  $L = 129.6$  mm. The diameter of the cylindrical model is  $D = 108$  mm

seen in the table. Especially for helium these differences become significant, because of much lower helium molar mass. This should move the high-speed boundary of the mixing layer somewhat closer to the nozzle axis, as compared to Vulcain 2. The kinetic energy ratio  $\rho_e u_e^2 / \rho_\infty u_\infty^2$  is 6 times smaller for both working gases compared to the Vulcain 2. But the total energy ratio  $e_{t,e} / e_{t,\infty}$  (kinetic energy and inner energy) is roughly similar for helium as working gas. Note that the molecular viscosity at high Reynolds numbers is not important for shear flow simulation.

### 3 Experimental setup

#### 3.1 Windtunnel HLB

Figure 2 displays the Hypersonic Ludwig Tube Braunschweig (HLB). The HLB is a cold Ludwig tube blow-down tunnel with a fast-acting valve. This valve separates the high-pressure and the low-pressure parts of the facility. The high-pressure part consists of the 17-m-long storage tube with a 3 m heated part. The maximum pressure in the storage tube is 30 bar. The low-pressure part consists of the wind tunnel nozzle, the 0.5 m circular test section, the diffuser and the dump tank. Two configurations are available. The hypersonic configuration is shown in Fig. 2a with a  $M = 5.9$  Laval nozzle. Figure 2b shows the supersonic tandem nozzle configuration. This configuration consists of a first nozzle, the settling chamber and the second  $M = 2.9$  Laval nozzle. Into the settling chamber a system of three perforated plates and discs of steel wool are integrated to improve uniformity of the flow upstream of the second nozzle. Prior to running the facility the low-pressure section is evacuated to a few mbar. The measuring time is about 80 ms with almost constant flow conditions. The unit Reynolds number range of the hypersonic configuration is

$Re = (3-20) \times 10^6$  1/m and for the supersonic configuration  $Re = (1.2-17.6) \times 10^6$  1/m. More detailed information on the design and operation of the HLB are given by Estorf et al. [32] and Wu et al. [33, 34].

#### 3.2 Design of jet simulation facility and wind tunnel model

Figure 3 shows a sketch of the jet simulation facility. The jet simulation facility is mounted in the test section using a steel support. The shape of the support is a  $30^\circ$  wedge followed by a flat part (length 156 mm, width 22 mm) and a  $20^\circ$  wedge. In order to trigger the transition of the boundary layer to a turbulent state a tripping is placed 98 mm behind the nose. The tripping material is carborundum with a grain size of  $400 \mu\text{m}$  and a width of 5 mm. The working principle is similar to the HLB wind tunnel itself. Outside of the HLB test section is the 32-m-long heated storage tube. The diameter of the storage tube is 18.9 mm and it can be pressurized up to 140 bar and heated up to 900 K. The rocket model is placed along the centerline of the HLB test section. A tandem nozzle, consisting of the first nozzle, the settling chamber and the second nozzle, is integrated into the rocket model. The second nozzle is an axisymmetric truncated ideal nozzle (TIC) with a mean exit Mach number,  $M_e = 2.5$ , and a nozzle exit diameter of  $d_e = 43$  mm, as designed by D. Saile [35] using Gruemmer's method [36]. The nozzle is designed for the working gas air with a design Mach number  $M_{\text{Design}} = 2.65$  and then truncated. The throat to exit area ratio is  $A/A^* = 2.64$  and the wall contour exit angle is  $4.8^\circ$ . The diameter of the settling chamber is  $d_{\text{SC}} = 39$  mm. A system of three perforated plates is integrated in the settling chamber to improve uniformity of the flow upstream of the second nozzle.

For scaling the afterbody the nozzle to body diameter ratio is used. For the Ariane 5 the nozzle diameter is



**Table 3** Kulite sensors used for unsteady pressure measurements

#	Sensor serial no.	Sensor type	Sensor position			Campaign	Built-in
			$x/D$	$r/D$	$\varphi, ^\circ$		
1	78	XCS-093	0	0.42	180 (I) 190 (II)	I, II	Base
2	93	XCQ-093	0	0.42	180 (II)	II	Base
3	77	XCS-093	0	0.42	190 (I) 240 (II)	I, II	Base
4	76	XCS-093	0	0.42	240 (I)	I	Base
5	27	XCS-LE-062	0.77	0.2	180	I	Nozzle
6	167	XCS-LE-062	0.77	0.2	180	II	Nozzle

$d_{\text{Ariane}} = 2.094$  m, and the body diameter is  $D_{\text{Ariane}} = 5.4$  m and hence, the ratio is  $d_{\text{Ariane}}/D_{\text{Ariane}} = 0.388$ . The Ariane nozzle lip thickness is 2.5 mm and therefore negligible. The diameter of the cylindrical body is  $D = 108$  mm while the model nozzle lip thickness is 0.5 mm. Therefore, the ratio is given for the inner and outer nozzle diameter. With the inner nozzle diameter  $d_{\text{inner}} = 42$  mm the ratio is  $d_{\text{inner}}/D = 0.389$ , while with the outer nozzle diameter  $d_{\text{outer}} = 43$  mm the ratio is  $d_{\text{outer}}/D = 0.398$ . Note that the external nozzle fairing length to body ratio  $L/D = 1.2$  represents the Ariane 5 value as well.

After the start of the facility the flow detaches in the first nozzle and a shock system is generated. Because of this shock system the flow is decelerated to subsonic speed, at the entry of the settling chamber. In the settling chamber the flow uniformity is improved with perforated plates designed to reduce total pressure and to work as flow straighteners, see Fig. 3. In the second nozzle the flow is accelerated to  $M_e = 2.5$  at the nozzle exit. Table 2 shows the freestream and jet simulation parameters for the supersonic and hypersonic configurations based on the jet simulation design according to chapter 2.

### 3.3 Instrumentation

The locations of the storage tube pressure sensor and the sensors in the settling chamber are shown in Fig. 3. A Gefran (Type: TKDA-N-1-Z-B16D-M-V) transducer is used for measuring the storage tube static pressure. The pressure range is between 0 and 160 bar and the response time for this transducer is less than 1 ms. For measuring the static pressure in the settling chamber three Kulites (XCEL-152) are used. The pressure ranges of these transducers are between 0 and 34.5 bar. The response time is less than 1 ms. The transducers are placed at the circumference with a  $120^\circ$  distance beginning from the top. They measure the static pressure in the settling chamber downstream of the perforated plates. The settling chamber total pressure  $p_{t,SC}$  is calculated using one-dimensional compressible flow

theory for a fixed Mach number in the settling chamber,  $M_{SC} = 0.26$ . Also in the settling chamber three temperature sensors are placed at the circumference with a  $120^\circ$  angular spacing beginning from the bottom. K-Type thermocouples (TJC100-CASS-IM025E-65 Sensor from Omega) are used for measuring the settling chamber total temperature. The sensitive wire junction is placed into the flow with a 10 mm distance from the settling chamber wall. The response time of the thermocouple, with an exposed 0.04 mm diameter wire is less than 20 ms. The total pressure at the nozzle exit is measured with a pitot rake consisting of 13 sensors. One sensor is located in the center of the nozzle exit. The other sensors are evenly distributed in two orthogonal bars. The distance between the sensors is 9 mm. Small and low-cost transducers from Honeywell (True Stability Silicon Pressure Sensors Series Standard Accuracy), with a pressure range from 0 to 10 bar and 1 ms response time, are used in the pitot rake.

For the unsteady base pressure measurement 4 Kulite sensors are flush mounted on the base and on the nozzle surface as seen in Fig. 3 (right). At the base, 3 Kulite sensors (Type: XCS-093, XCS-093, pressure range 0.35 bar absolute) are placed at the circumference at  $180^\circ$ ,  $190^\circ$ , and  $240^\circ$ , measured with respect to the top location. The distance from the centerline is 45 mm. Another Kulite sensor is placed on the nozzle fairing at  $180^\circ$  and 83 mm downstream of the base. The used sensors are listed in Table 3. The sensor locations are chosen following the previous studies by Saile et al. [27, 28]. The radial position from the centerline  $r/D = 0.42$  is limited by the facility itself. The first circumference position ( $180^\circ$ ) is chosen on the side opposing the facility support. The other circumference positions ( $190^\circ$ ,  $240^\circ$ ) are chosen to cover the fluctuation decrease on the base along the circumference. The fairing sensor is placed as far as possible downstream. At this location high dynamic loads are expected on the nozzle structure.

The pressure data were sampled with a Spectrum M2i.4652 transient recorder. The sampling frequency was set to 3 MHz and fluctuations under 200 Hz and above

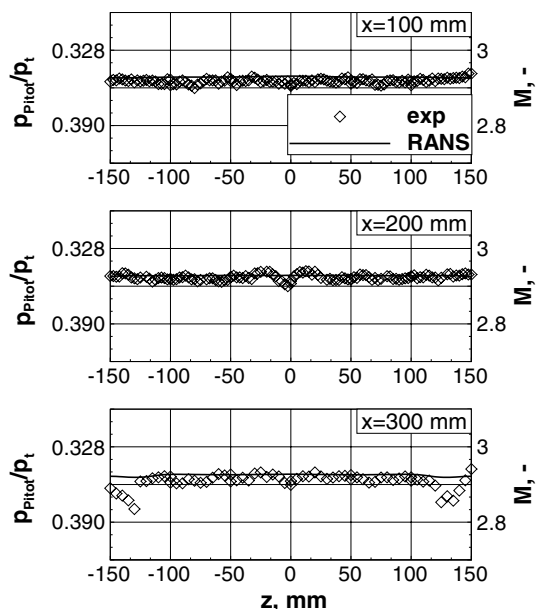


Fig. 4 Pitot pressure and Mach number distribution for the supersonic configuration ( $M = 2.9$ )

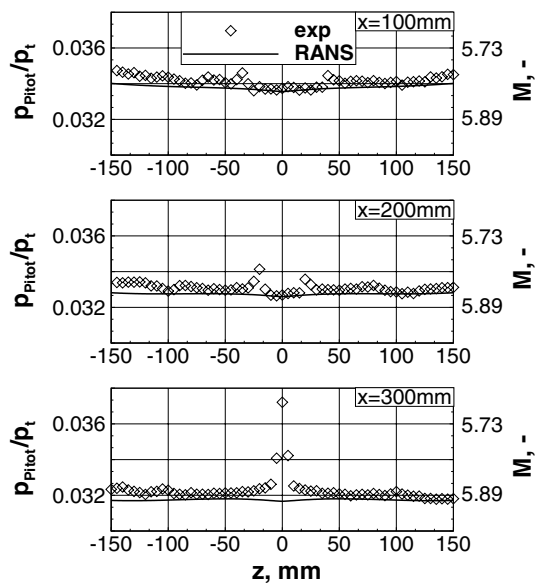


Fig. 5 Pitot pressure and Mach number distribution for the hypersonic configuration ( $M = 5.9$ ) [32]

50 kHz were removed by applying a filter. The power spectral density (PSD) is computed using Welch’s method. The PSD are based on 40 ms time traces. The time traces of 10 tunnel runs are merged to obtain resolved spectra. For the analysis the data was segmented into sets of 120,000 points with a 50 % overlap. The obtained frequency resolution is  $\Delta f = 25$  Hz. Each window was multiplied with a normalized Hamming window.

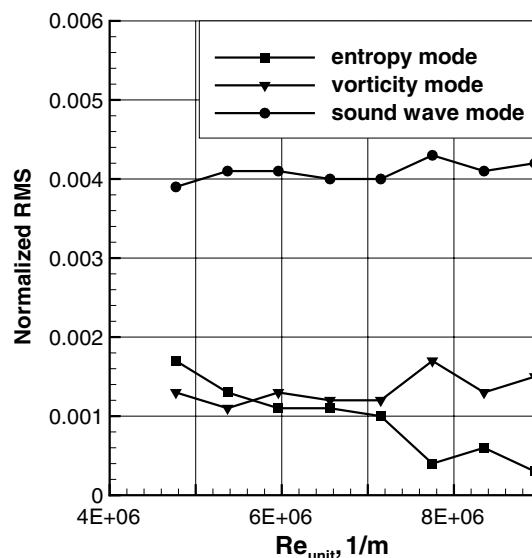


Fig. 6 Modal analysis of flow quality in supersonic flow ( $M = 2.9$ )

## 4 Flow quality

### 4.1 Windtunnel

Figures 4 and 5 show the measured and computed pitot pressure and Mach number distributions in the wind tunnel test section. The measurements are conducted in vertical direction from  $z = \pm 150$  mm and at different axial positions downstream of the nozzle exit ( $x = 0$  mm). The distributions for the supersonic configuration are given in Fig. 4. The decrease at the position around  $z = \pm 150$  mm,  $x = 300$  mm shows the shock wave due to the test section wall. The results for the hypersonic configuration, shown in Fig. 5, were previously provided by Estorf [32]. The peaks at  $z = \pm 30$  mm,  $x = 100$  mm,  $z = \pm 20$  mm,  $x = 200$  mm and the center  $z = 0$  mm,  $x = 300$  mm shows the interaction of a shock wave due to the Pitot probe and a weak conical shock wave. The origin of the conical shock wave is most likely a minor contour discontinuity between the steel nozzle throat and the glass reinforced plastic nozzle [32]. Both figures show a good agreement between the computed and the measured distributions. The distributions represent almost constant Mach numbers along the test section and symmetrical flow fields.

To characterize the disturbances of the flow field, the combined modal analysis theory is employed [38]. By using a Pitot probe together with hot-wire anemometry, the disturbances of the freestream are decomposed into three different modes, entropy mode, vorticity mode and sound wave mode [39, 40]. The origin of the three disturbance modes is different. The entropy disturbances and the

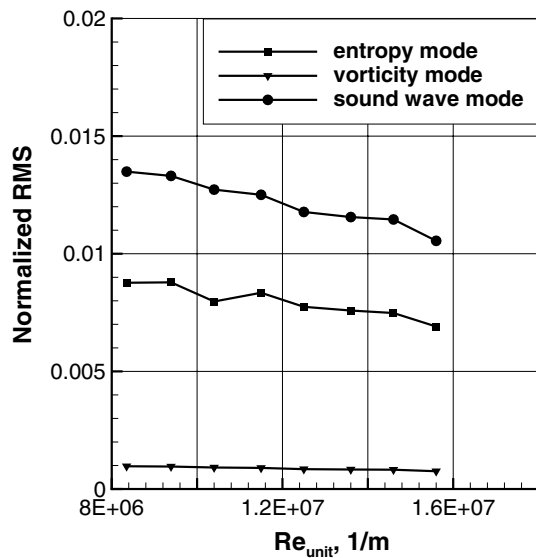


Fig. 7 Modal analysis of flow quality in hypersonic flow ( $M = 5.9$ )

vorticity disturbances are transmitted from the upstream sections, such as the control valve and the settling chamber. The acoustic waves are the most important in supersonic and hypersonic tunnels. They appear as eddy Mach waves, shivering Mach waves, and flow noise transmitted from upstream installations of the wind tunnel. The former is flow noise generated by the turbulent boundary layer of the wind tunnel nozzle. The shivering Mach wave is generated as reflection or diffraction of steady pressure gradients from the turbulent boundary layer of the tunnel nozzle. This wave hence originates from imperfections of the wind tunnel nozzle. The objective is to qualify all three disturbance modes individually. A hot-wire probe is sensitive to mass flow and temperature fluctuations, together with the Pitot probe, the fluctuations of entropy mode  $\theta$ , vorticity mode  $\omega$ , and sound wave mode  $\sigma$  can be obtained with the combined modal approach.

$$\sigma' = \frac{P'}{\gamma \bar{P}}; \quad \omega' = \frac{\alpha}{\alpha + \beta} \frac{m'}{\bar{m}} + \frac{1}{\alpha + \beta} \frac{T_0'}{T_0} - \left[ \frac{\alpha}{\alpha + \beta} + \frac{n_x}{\gamma M} \right] \frac{P'}{\bar{P}}$$

$$\theta' = -\frac{\beta}{\alpha + \beta} \frac{m'}{\bar{m}} + \frac{1}{\alpha + \beta} \frac{T_0'}{T_0} - \left[ \frac{\alpha}{\alpha + \beta} + \frac{2n_x}{\gamma M} + \frac{1}{\gamma} \right] \frac{P'}{\bar{P}},$$

with  $\alpha = [1 + (\gamma - 1)/2] M^2]^{-1}$ ,  $\beta = \alpha (\gamma - 1) M^2$ , and  $n_x$  is the direction cosine of the normal to the plane wave. In the present case,  $n_x$  is 0.4 when Mach number is 3 and 0.6 when the Mach number is 6 according to the Laufer's investigation [41].  $m$ ,  $p$ ,  $T_0$  are mass flow, pressure and total temperature, respectively. The prime denotes the fluctuating component, whereas the overbar means the mean component of the flow variables. The static pressure fluctuation can be obtained from the Pitot probe measurement based

on the estimation of Stainback [42]. The resultant fluctuations are depicted in Figs. 6 and 7. In the supersonic flow, the sound wave mode is the dominating disturbance, whereas the other two modes are relatively low. Obviously, the wind tunnel is acoustic wave dominated when it is operated in Mach 2.9 with cold air. For hypersonic flow, the disturbance displays different behavior that the sound wave mode decreases with the Reynolds number, whereas the entropy mode and the vorticity mode appear rather independent of Reynolds number. In particular, the entropy mode hereby is relatively high since the tunnel is operated with a heated storage tube for Mach 5.9 flow. Note that larger unit Reynolds numbers lead to a smaller sound wave mode, which is typical for an acoustic wave dominated wind tunnel. It appears that the entropy mode is of similar order than the sound wave mode. That leaves some uncertainty on the absolute levels of sound wave mode and entropy mode since the assumption of vanishing interactions between the two modes becomes questionable. For a comparison to other conventional wind tunnels usually the normalized Pitot pressure fluctuation is used. The normalized Pitot pressure fluctuation is about 0.57 % for the supersonic flow and about 1.8 % for the hypersonic flow. Overall, the results show good flow quality in supersonic and hypersonic flow compared to other conventional wind tunnels [34].

## 4.2 Jet simulation facility

For qualifying the jet simulation facility, a series of measurements with varying operation parameters was conducted. At least five tunnel runs were done for each flow condition and the transients during each tunnel run were evaluated. The pressure and the temperature in the settling chamber and the pitot pressure at the nozzle exit were measured for two different storage tube pressures ( $p_0 = 80$  and  $p_0 = 140$  bar) and for different storage tube temperatures ( $T_0 = 300$  and  $T_0 = 900$  K). Also the pitot pressure distributions in the jet plume flow with surrounding flow for two axial positions were measured. Here, the storage tube pressure of the jet simulation was  $p_0 = 140$  bar and the temperature was  $T_{SC} = 470$  K and  $T_{SC} = 620$  K. The flow properties of the surrounding flow are described by  $p_{t,\infty} = 16.79$  bar,  $T_{t,\infty} = 470$  K,  $M_\infty = 5.9$ . The working gas for the HLB and the jet simulation facility was air. During these initial tests and the surrounding initial pressure in the HLB test section was always less than 6 mbar.

### 4.2.1 Flow measurements in storage tube and settling chamber

Figure 8 shows the static storage tube pressure for different initial storage tube pressures and different temperatures.



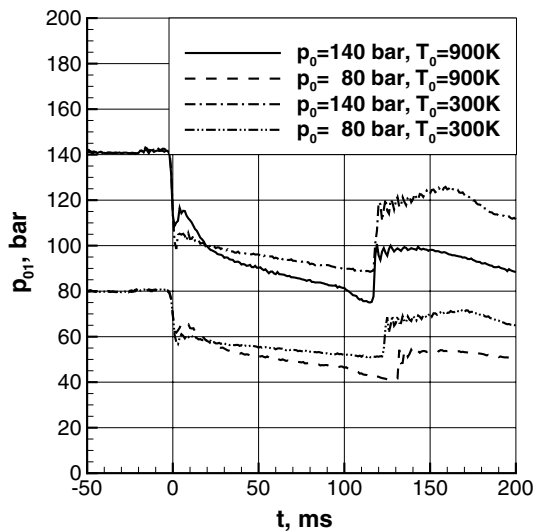


**Fig. 8** Static storage tube pressure for different initial storage tube pressures and different storage tube temperatures

Right after the opening of the fast-acting valve ( $t = 0$  ms) there is a pressure loss of 24 % for low temperatures and of 26 % for high temperatures because of the unsteady starting process. During the measuring time of 100 ms the pressure drops further by 15 %. This pressure loss can be described by the pressure drop in a pipe. The length of pipe flow behind the expansion wave within the storage tube increases during run time of the jet simulation facility, and hence the pressure loss increases as well. The pressure drop in a turbulent pipe depends mainly of the fluid density and the square of the flow velocity. While the storage tube Mach number of HLB wind tunnel is around 0.06, the storage-tube Mach number of the jet simulation facility is 0.2, which is defined by the area ratio of first throat and tube. Therefore, the jet simulation storage-tube flow generates significant pressure losses, compared to the wind tunnel storage tube. By increasing the jet temperature, the speed of sound in the storage tube increases and therefore the pressure loss increases as well. Note that the pressure loss is expected to increase by using helium as working gas due the higher speed of sound.

In Fig. 8 there is a further decrease of the pressure seen after about 100 ms. This pressure drop indicates the maximum operating time of the jet simulation facility that depends on the storage tube temperature. It is found that after 100 ms the expansion wave from the starting process appears back in the valve section. Note that the measuring time depends on the speed of sound and hence on the storage tube temperature. The ratio of settling chamber pressure to storage tube pressure during runtime is shown in Fig. 9. The ratio is constant over time, but at higher temperature its value is lower. This ratio illustrates the strong

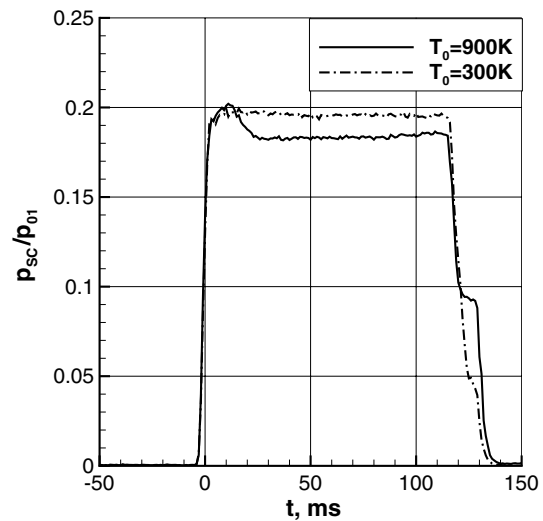


**Fig. 9** Settling chamber pressure to storage tube pressure during runtime for different temperatures

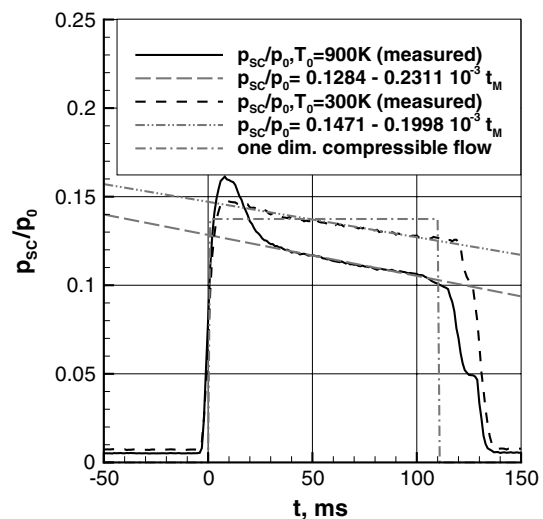


**Fig. 10** Settling chamber pressure to initial storage tube pressure ratio (measured, calculated and linear function over measuring time)

pressure loss between the storage tube and the end of the settling chamber. The initial pressure loss agrees well with preliminary estimates based on one-dimensional compressible flow theory. Figure 10 shows the ratio of settling chamber pressure to initial storage tube pressure for different storage tube temperatures. The dash-dot curve shows the pressure ratio calculated with one-dimensional compressible flow theory. The dashed and the solid curves show the measured ratios for low and high storage tube temperatures. The experimentally obtained settling chamber pressure can be well described with a linear function

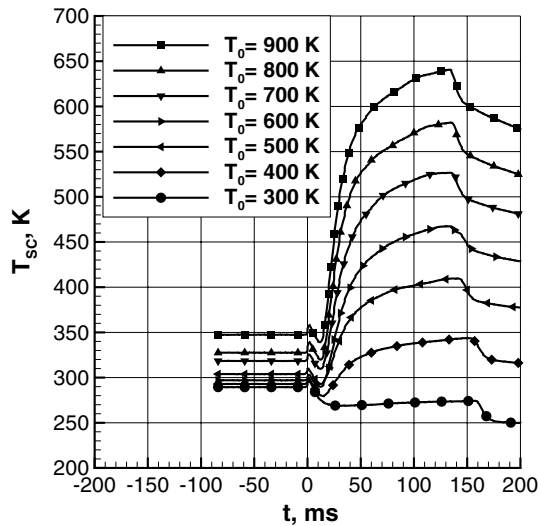


**Fig. 11** Settling chamber temperatures at varied storage tube temperatures ( $p_0 = 140$  bar)

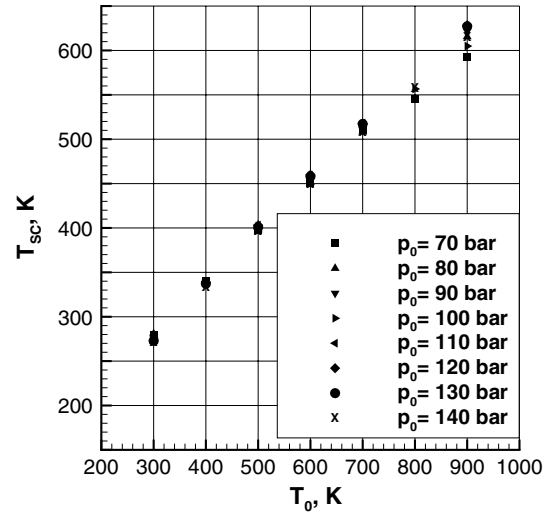


**Fig. 13** Settling chamber temperatures for different storage tube temperatures at 80 ms

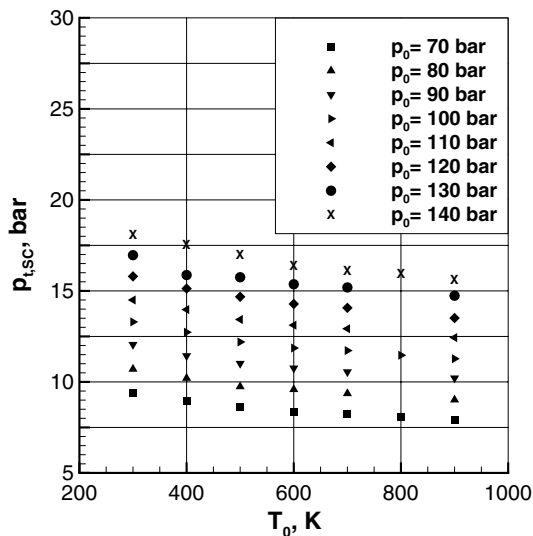


**Fig. 12** Settling chamber pressure for different storage tube temperatures at 80 ms

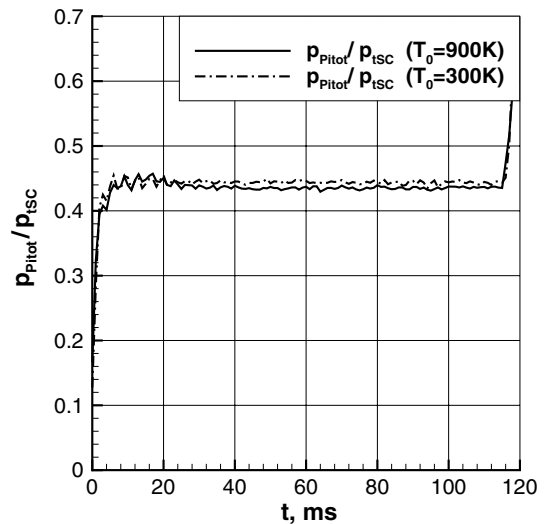


**Fig. 14** Pitot pressure in the center of the rocket nozzle exit

in dependence of the initial storage tube pressure and the measuring time.

Figure 11 shows the measured temperature in the settling chamber over run time for a storage tube pressure  $p_0 = 140$  bar and for different storage tube temperatures. For a storage tube temperature of  $T_0 = 900$  K the total temperature in the settling chamber reaches  $T_{sc} = 620$  K after 80 ms. We find that for high storage tube temperatures the settling chamber does not reach a constant level. This could be caused by heat transfer in the unheated support tube that connects the model with the heated storage tube.

Figure 12 shows the settling chamber total pressure  $p_{t,sc}$  as a function of storage tube temperature  $T_0$  and storage tube pressure taken at 80 ms after the facility start. With higher storage tube temperatures the settling chamber pressure decreases. Figure 13 displays the settling chamber temperature as function of the storage tube temperature for storage tube pressures from 70 to 140 bar (80 ms after the facility starts). Up to  $T_0 = 700$  K the variance of the settling chamber temperature is  $\pm 10$  K. For higher storage tube temperatures the temperatures variances increase.

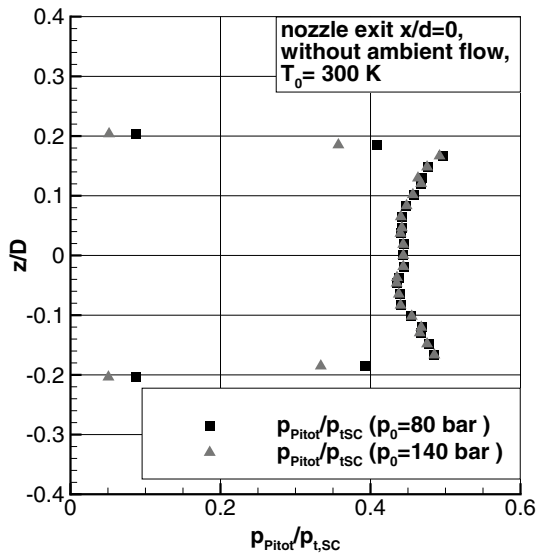


Fig. 15 Pitot pressure distribution along the vertical nozzle exit

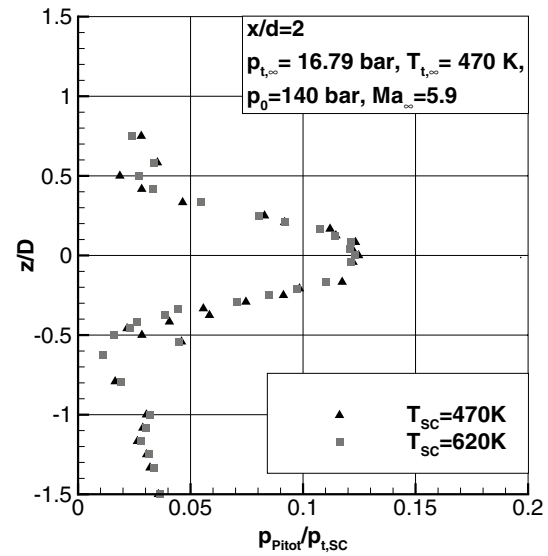


Fig. 17 Pitot pressure distribution in jet plume at  $x/d = 2$

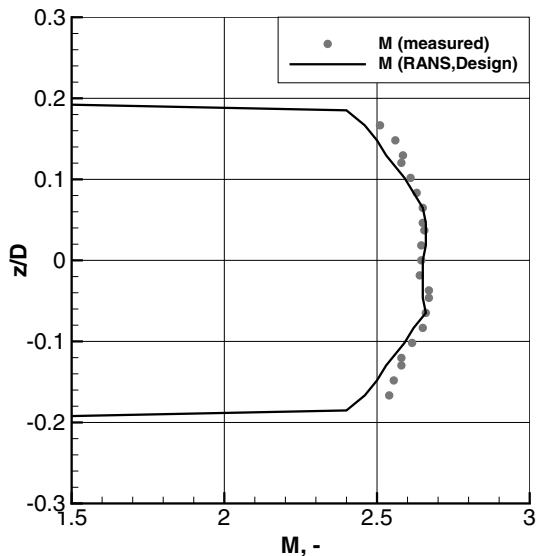


Fig. 16 Pitot pressure distribution in the vertical plane of symmetry at the nozzle exit

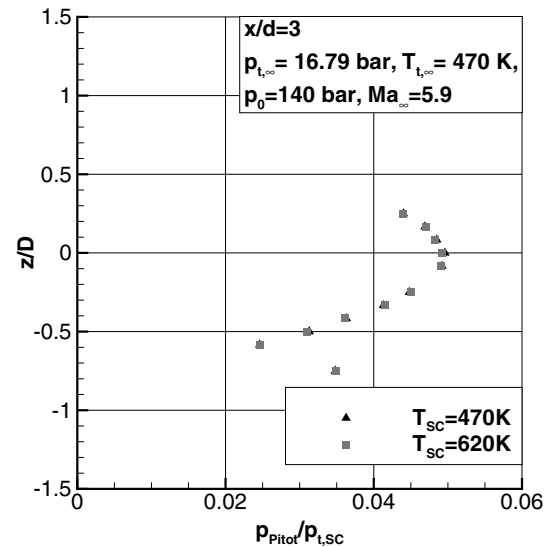


Fig. 18 Pitot pressure distribution in jet plume  $x/d = 3$

#### 4.2.2 Flow measurements of propulsive jet

Figure 14 shows the ratio of nozzle exit pitot pressure to settling chamber total pressure ratio. The pitot pressures are measured in the center of the nozzle exit as an average over 5 tunnel runs. The values are almost constant over the measuring time. We find

$$\begin{aligned}
 p_{Pitot,C} &= (0.4440 \pm 0.0033) \cdot p_{t,SC}(T_0 = 300 \text{ K}) \\
 p_{Pitot,C} &= (0.4357 \pm 0.0044) \cdot p_{t,SC}(T_0 = 900 \text{ K}). \quad (1)
 \end{aligned}$$

Figure 15 shows the vertical pitot pressure distribution across the nozzle exit. The distribution indicates an almost

symmetrical jet flow. Also it is shown, that the pressure increases in radial direction. In Fig. 16 the Mach number distribution calculated with the Rayleigh pitot formula is shown. Also the Mach number distribution obtained from RANS computations of the same nozzle by Saile [35] is included. The figure shows a good agreement between the computed and the measured Mach number distribution. In Figs. 17 and 18 the measured pitot pressure distributions of the plume flow at the axial positions  $x/d = 2$  and  $x/d = 3$  are shown. The storage tube pressure was  $p_0 = 140$  bar and the settling chamber temperatures were varied between 470 and 620 K. The flow properties of the surrounding flow were  $p_{t,\infty} = 16.79$  bar,  $T_{\infty} = 470$  K and



**Fig. 19** Averaged Schlieren image without jet flow ( $p_{t,\infty} = 1.5$  bar,  $T_\infty = 285$  K and  $M_\infty = 2.9$ )

$M_\infty = 5.9$ . Both facilities were synchronized to overlap their measuring windows. The values used for the evaluation are the mean values between 60 and 80 ms after the start of the jet simulation facility. Figure 17 shows the pitot pressure distribution of the plume flow at the axial position  $x/d = 2$ . Note that the differences between the pitot pressure distributions at different temperatures may have also been affected by locally large variations from run to run in the mixing region at  $z/D = \pm(0.4-1)$  that divides the jet flow from the surrounding flow. In Fig. 18 the pitot pressure distribution for the axial position  $x/d = 3$  is shown. These measurements were only conducted for the lower part of the jet plume.

## 5 Afterbody flow analysis

For the analysis of the afterbody flow Schlieren images were obtained and the unsteady base pressure was measured with and without jet flow. The results for the supersonic and hypersonic configuration with different jet temperatures are discussed. The supersonic flow properties for the surrounding flow are described by  $p_{t,\infty} = 1.5$  bar,  $T_{t,\infty} = 285$  K,  $M_\infty = 2.9$  and  $Re = 12 \times 10^6$  1/m. The jet total pressure was  $p_{t,SC} = 4.1$  bar and the settling chamber temperature was varied as 280, 470, 620 K. The external flow properties for the hypersonic configuration are described by  $p_{t,\infty} = 16.79$  bar,  $T_{t,\infty} = 470$  K,  $M_\infty = 5.9$  and  $Re = 16 \times 10^6$  1/m. The jet temperature was also varied as 280, 470 and 620 K. The jet total pressure decrease slightly with higher temperatures [ $p_{t,SC} = 20.4$  bar (280 K),  $p_{t,SC} = 18.8$  bar (470 K),  $p_{t,SC} = 17.5$  bar (620 K)], see Sect. 4. Note that the given values are measured 40 ms after tunnel start.

The measurements were conducted in two campaigns. In the first campaign the hypersonic configuration was tested. During the second campaign the hypersonic measurements

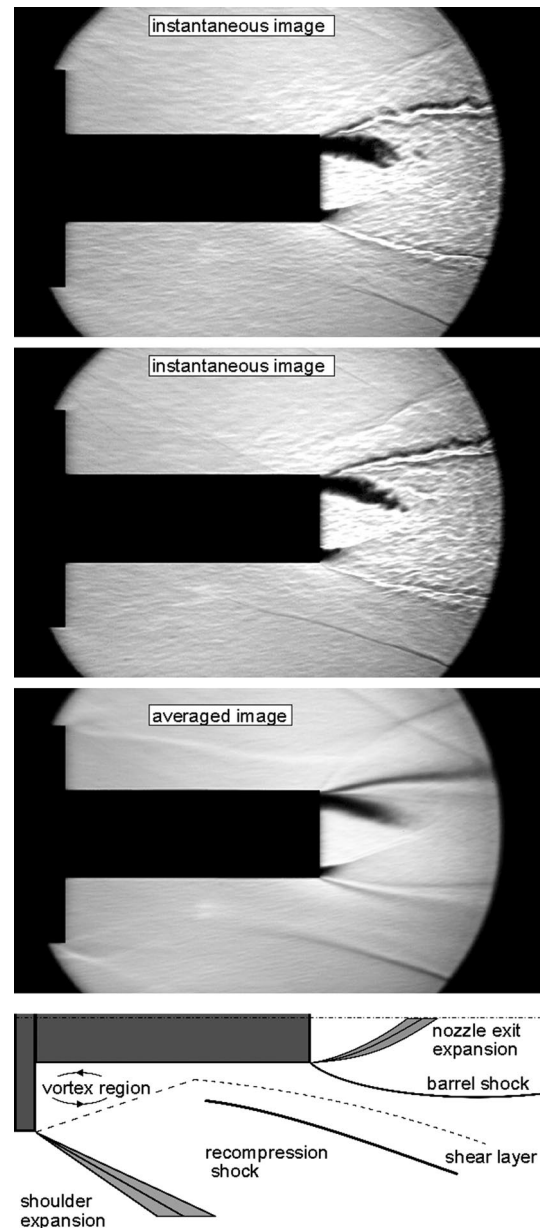


**Fig. 20** Instantaneous and averaged schlieren image with jet and surrounding flow ( $p_{t,sc} = 4.1$  bar,  $T_{SC} = 280$  K and  $M_e = 2.5$ ,  $p_{t,\infty} = 1.5$  bar,  $T_\infty = 285$  K and  $M_\infty = 2.9$ ) and a sketch of the mean base flow features

were repeated and the supersonic configuration was tested. Additionally, the position and the type of the Kulite sensors were also varied, see Table 3.

### 5.1 Mean afterbody flow

The rocket afterbody flow field was characterized by using Schlieren pictures. The presented pictures show the average over 150 instantaneous pictures. Figures 19 and 20 show the supersonic configuration with and without the jet. In

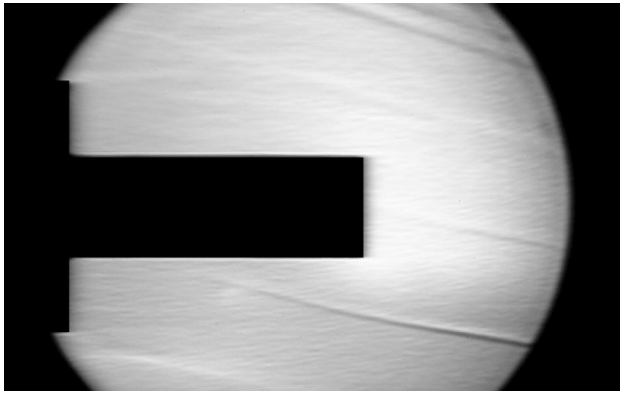


**Fig. 21** Averaged schlieren image without jet flow ( $p_{t,\infty} = 16.79$  bar,  $T_\infty = 470$  K and  $M_\infty = 5.9$ )

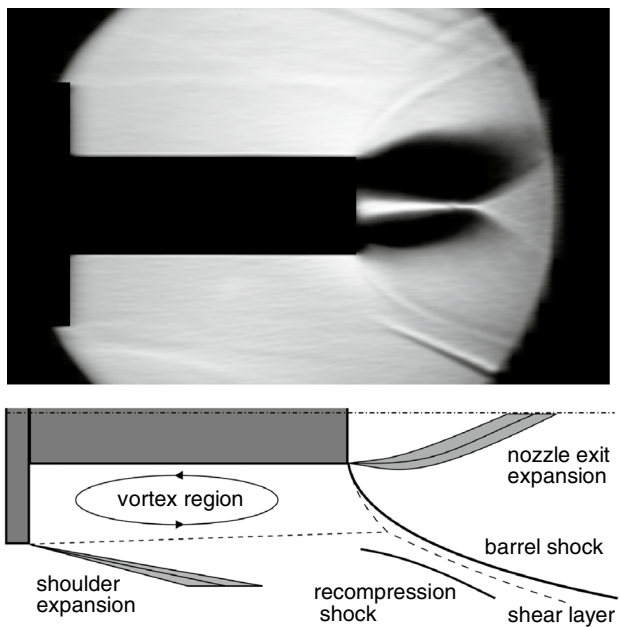


**Fig. 22** Averaged schlieren image with jet and surrounding flow ( $p_{t,sc} = 18.8$  bar,  $T_{SC} = 470$  K and  $M_e = 2.5$ ,  $p_{t,\infty} = 16.79$  bar,  $T_\infty = 470$  K and  $M_\infty = 5.9$ ) and a sketch of the mean base flow features

the lower part of Fig. 19 the recompression shock of the external flow is visible. Figure 20 shows that the recompression shock is slightly displaced by the under-expanded plume. Also the jet expansion fan, the plume barrel shock and the first jet shock cell are visible. The jet mixing area is between the barrel shock and the outer compression shock. The instantaneous pictures show the fluctuation of the barrel shock due to the freestream flow. The Schlieren pictures for the hypersonic configuration are given in Figs. 21 and 22. Figure 21 shows the Schlieren image without jet. The recompression shock is also visible in the lower part.

Compared to the supersonic configuration there are little differences in the recompression shock shape. However, with propulsive jet the recompression shock is significantly displaced by the strongly under-expanded jet as shown in Fig. 22. Also the jet characteristics such as the jet expansion fan, the plume barrel shock and as well the jet mixing area are visible. The flow near the nozzle lip (exit) is strongly over-expanded. Due to this expansion fan, there are large density gradients. The Schlieren images visualize such density gradients. However, when these gradients are large enough the light rays can be deflected that much that they are blocked by the knife edge. This phenomena causes the dark structure in the Schlieren image of Fig. 22. In the upper part the light rays are deflected into the opposite direction. Hence, the dark structure appears differently. This effect could reduce by changing the orientation of the Schlieren edge or using a round Schlieren edge. In this case the orientation is held horizontal hence the supersonic and hypersonic pictures are comparable. The oblique waves in the upper part of the flow are most likely caused by the model support.

Figures 23 and 24 show the normalized mean afterbody pressures for  $M_\infty = 2.9$  and  $M_\infty = 5.9$ , respectively. The mean base pressure is about 30 % ( $M_\infty = 2.9$ ) and 20 % ( $M_\infty = 5.9$ ) of the freestream pressure without jet flow. The mean pressure on the fairing is in the order of the freestream pressure. This indicates that the flow is reattached at the nozzle fairing. With jet flow the mean pressures at the base increase while they decrease at the nozzle fairing. That implies that the reattachment of the outer flow (recompression shock) is displaced by the under-expanded plume. For the supersonic configuration the pressure change is rather small regarding to the slightly under-expanded plume, see Fig. 20. For the hypersonic configuration the degree of the under-expansion is much higher. Therefore, the mean pressure increase and decrease is higher compared to the supersonic configuration. The recirculation area is more strongly influenced by the under-expanded plume. The mean base and nozzle fairing pressures are now rather similar at the hypersonic configuration. That implies that the outer flow is not reattached on the nozzle fairing and the recirculation area reaches from the base to the nozzle.

The effect of an over-expanded jet is described by Deprés et al. [15]. They mention that wall pressure decreases due the suction effect of the jet shear layer by the presence of a jet. A reduction of the nozzle pressure ratio reduces this effect as the smaller jet radius induces a smaller circumferential surface of the jet shear layer. Also the fluctuation level increases with increasing nozzle pressure ratio. Sahu [13] investigated the effect of a slightly under-expanded jet over a boattailed missile afterbody and found that the base pressure increases with an increasing degree of under-expansion.



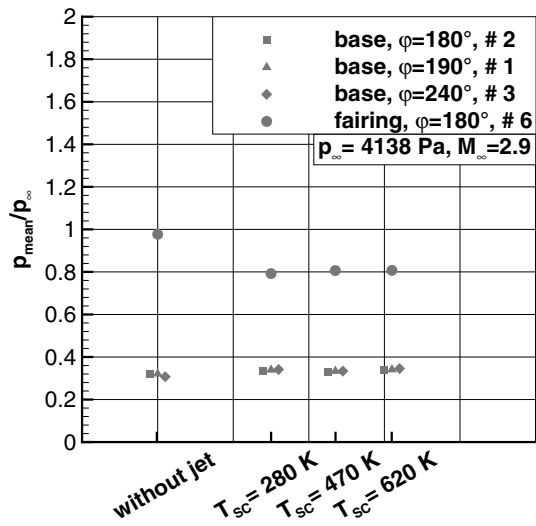


**Fig. 23** Normalized base and nozzle fairing pressure with and without jet.  $M_{\infty} = 2.9$

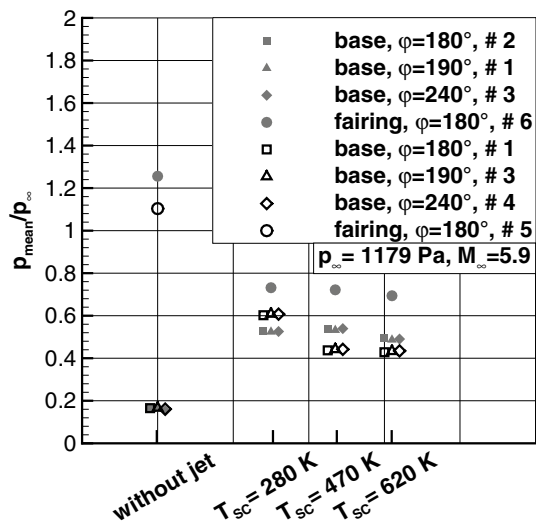


**Fig. 24** Normalized base and nozzle fairing pressure with and without jet.  $M_{\infty} = 5.9$

In the present study, the effect by an under-expanded jet is observed. Due to an increasing degree of under-expansion the mean base pressure increases and the fairing pressure decreases as shown in Figs. 23 and 24. The fluctuation levels  $p'_{\text{RMS}}$  increase on the base and decrease on the fairing due to the under-expanded plume, see Figs. 27, 28, 29, 30. This effect increases with to the degree of under-expansion and this is in line with the observations described by Déprés [15]. Obviously, the larger size of the jet radius due to the under-expanded jet induces a larger circumferential surface of the jet shear layer.

## 5.2 Unsteady afterbody flow

Figures 27, 28, 29 and 30 display the power spectral density (PSD) as measured by the Kulite sensors. The ordinate shows the PSD of the pressure fluctuation  $p' = p - p_M$  in  $\text{Pa}^2/\text{s}$  and the abscissa denotes the non-dimensional Strouhal number. Note that the PSD, with the unit  $\text{Pa}^2/\text{s}$ , is calculated using the non-dimensional Strouhal number. The Strouhal number is defined as  $St = D f / u_{\infty}$  with the rocket body diameter  $D = 0.108$  m, the frequency  $f$  and the freestream flow velocity  $u_{\infty} = 910.5$  m/s ( $M_{\infty} = 5.9$ ) and  $u_{\infty} = 606.7$  m/s ( $M_{\infty} = 2.9$ ). All Figures display spectra with and without jet flow. With jet flow the settling chamber temperature and therefore the jet exhaust velocity is varied. The jet exit velocity is  $u_{\text{jet},280\text{K}} = 559$ ,  $u_{\text{jet},470\text{K}} = 724$  and  $u_{\text{jet},620\text{K}} = 832$  m/s, using the settling chamber temperatures and assuming one-dimensional nozzle flow. For each signal the corresponding fluctuation RMS value is also reported.

Note that Strouhal numbers above one are not critically relevant for real flight of launchers as Ariane 5 because the natural frequencies of the base/nozzle structure are significantly lower. However, for understanding fundamental base flow sensitivities fluctuations at high frequencies are important. It is further noted that that Ariane 5 launcher uses a conical nozzle fairing, whereas the present generic afterbody employs a cylindrical fairing. Since this geometrical change should not fundamentally change the topology of reverse flow and afterbody shear layer the authors assume that the present results are representative for rocket afterbodies with extended nozzle fairings.

## 5.3 Signal quality

The quality and the repeatability of the signals are also observed. Further the influence of removing and remounting of all sensors is shown. As quality characteristic, the RMS value of the pressure signal before each tunnel run (noise) is used. In the first campaign the RMS noise value of all base sensors are smaller than 2.3 Pa. This implies a possible resolution of fluctuations of 2.3 Pa. In the second campaign different types of sensors and positions, as shown in Table 3, are used. After remounting, the sensors 1 and 2 show similar RMS values below 2.3 Pa. Sensor 3 shows an increased RMS value up to 6.4 Pa due to the remounting. The fairing sensor 5 shows an RMS value up to 14 Pa and is therefore not applicable for fluctuation measurements. In the second campaign another sensor (6) is used on the fairing. This sensor shows an RMS value smaller than 2.1 Pa. In conclusion, all sensors except sensor 5 show a low RMS value and therefore a good signal quality. However, the spectra analysis of sensor 1 indicated a faulty transfer function for high frequencies. Therefore, sensor 1 is also not considered in the following discussions.

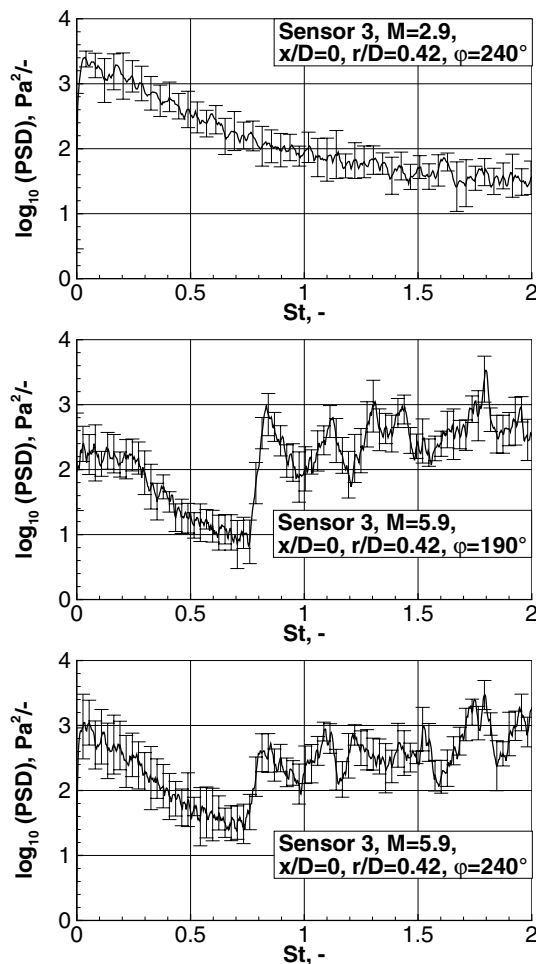


**Fig. 25** Spectra and standard deviation of sensor 3 at different sensor positions and configurations. Every tenth error bar is shown

Further the repeatability of the sensor 3 signal with jet ( $T_{SC} = 470$  K) is analyzed and shown in Fig. 25. This shows the logarithmic mean spectra and their standard deviations for different positions and configurations. The mean value and the standard deviation is calculated using 12 single measurements. The signals are smoothed using a moving average filter. The mean amplitude error is 12.6 % for the supersonic and 16.0 % for both hypersonic configurations. An additional effect of the repeatability after 1 year is shown in Fig. 28 (right column). The base sensor at  $\varphi = 240^\circ$  shows a significant amplitude drift after removing and remounting of all sensors. The origin of this shift is uncertain.

Figure 26 shows the unfiltered and filtered spectra of sensor 3 at different sensor positions and configurations. The unfiltered signal shows a peak at about 110 kHz due to the sensor natural frequency. Due to the natural frequency and in order to gain the physically relevant signal and the corresponding RMS values the signals are low-pass filtered at the cut-off frequency of  $f_c = 50$  kHz. The cut-off

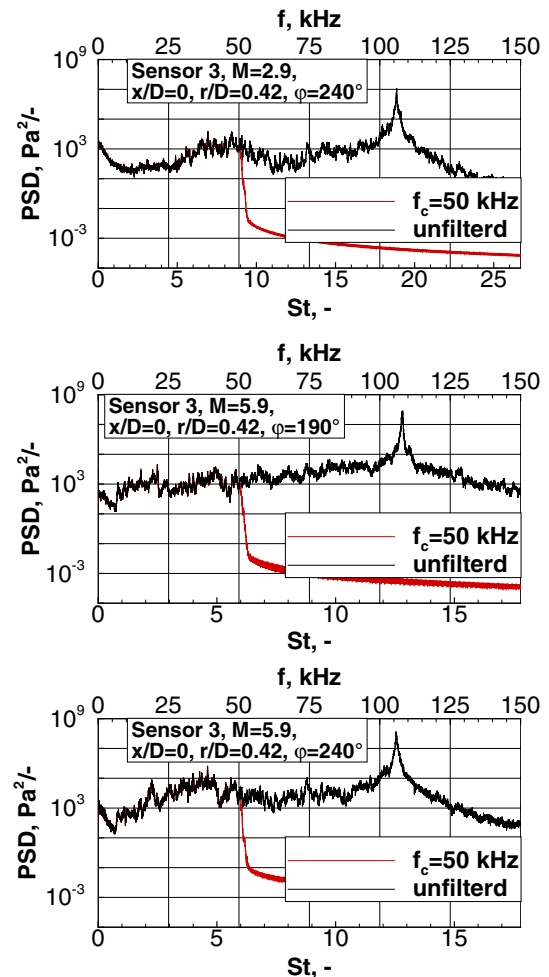


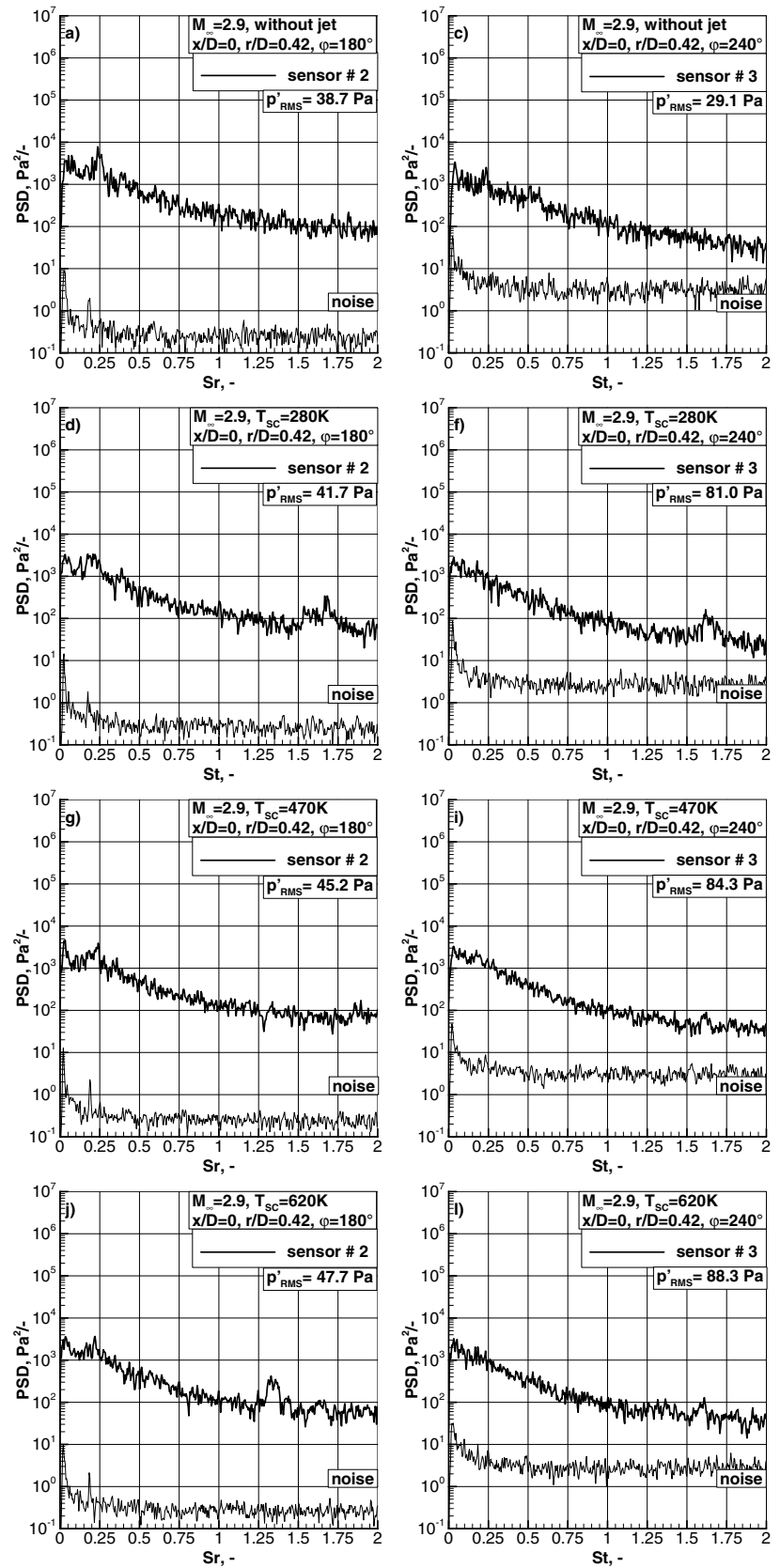
**Fig. 26** Unfiltered and filtered spectra of sensor 3 at different sensor positions and configurations. Cut of frequency  $f_c = 50$  kHz

frequency is much greater than the frequencies under consideration in this study.

### 5.3.1 Supersonic configuration

Figure 27 shows the results for the supersonic configuration. Column by column the different sensors and line by line the jet variations are given. A local peak in Strouhal number at  $St = 0.2-0.25$  is obtained for the  $180^\circ$  sensor. Along the circumference this peak decreases. The Strouhal number near  $St = 0.2$  points to the well-known “shedding”, respectively, the flapping motion of the von Kármán vortex street of a cylindrical body. This peak is found by several authors [6, 10, 15, 19]. For hypersonic base flows Statnikov et al. [25] and Saile et al. [28] found similar peaks. With jet flow we obtained an additional peak at higher Strouhal numbers. For lower settling chamber temperature/jet velocities this peak is near  $St \approx 1.6$  at both base positions. For higher temperatures/jet velocities this peak moves to lower

**Fig. 27** PSD at  $M_\infty = 2.9$  for base sensors. *Column* base sensor position. *Line* without jet and varied jet temperatures



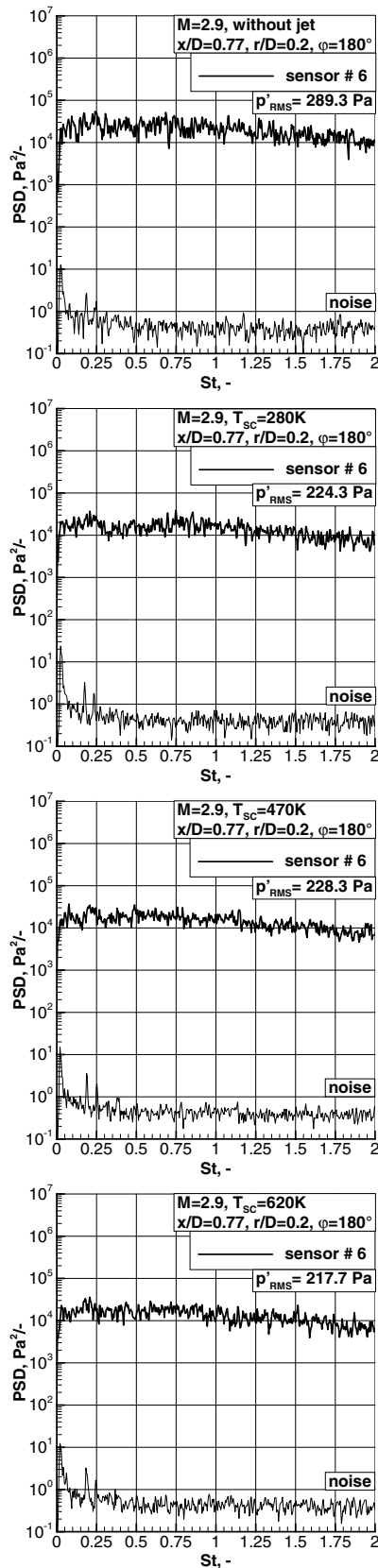


**Fig. 28** PSD at  $M_\infty = 2.9$  for nozzle fairing sensor. Line without jet and varied jet temperatures

Strouhal numbers  $St \approx 1.3$ . These peaks at higher Strouhal numbers may result from the high-energy motion of the shear layer. Figure 28 shows the spectra from the pressure fluctuations obtained from the nozzle fairing sensor. The fluctuation level is higher compared to the base sensors and no dominating peaks are observed.

### 5.3.2 Hypersonic configuration

Figure 29 displays the spectra obtained from the base sensors for the hypersonic configuration. Without jet flow a peak at  $St \approx 0.3$  is obtained. For the sensors at  $180^\circ$  and  $190^\circ$  this peak is well-marked. The peak decreases in circumference direction. Note that for  $St > 1$  the sensor noise and the signal are of the same order. With jet flow the peak shifts to lower Strouhal numbers between  $St = 0.2$  and  $0.25$ . These peaks near  $St \approx 0.2$  are also obtained by the supersonic configuration and belong to the well-known “shedding”. Stanikov et al. [26] associated this peak at  $St \approx 0.25$  with a longitudinal pumping of the cavity. With jet additional peaks at higher frequencies are found. A local peak at  $St \approx 0.6$  is obtained for  $T_{SC} = 280$  K. This peak may belong to the swinging mode of the shear layer found by Stanikov et al. [26] (sensor position: in the wake at  $x/D = 0.77$  and  $r/D = 0.44$ ). Our other sensors do not show this peak.

For frequencies higher than  $St \approx 0.75$  the fluctuation level increases strongly at all base sensors, with jet simulation. The reason for this large fluctuation level is the strongly under-expanded plume of the hypersonic configuration. The spectra in Fig. 29g–l show peaks near  $St = 0.8–0.9$ . These peaks may be related to a radial flapping motion of the shear layer [26]. An additional effect of the jet is a peak in the region of  $St \approx 1.1$  (all base sensors). This peak at  $St \approx 1.25$  increases with higher settling chamber temperature and hence jet velocities. For the sensor at position  $240^\circ$  the peaks at  $St \approx 1.1$  and  $St \approx 1.25$  appear merged. Further a peak at  $St \approx 1.55$  is found. This peak decreases with increasing settling chamber temperature/jet velocities. Finally, all base sensor spectra display a peak at  $St = 1.75–1.80$ . This peak is also detected with the nozzle fairing sensor, shown in Fig. 30. It increases on the base and on the fairing with higher settling chamber temperature/jet velocities. These peaks at high frequencies indicate a high-frequency motion of the shear layer. Without jet no peak is found on the nozzle fairing. With increasing jet temperature the fluctuation level increases. Saile et al. [28] did investigations on a similar generic rocket model configuration with jet flow and also found base pressure fluctuation peaks between  $St = 0.8$  and  $St = 1.1$ . The dominating peaks above  $St > 0.8$  are influenced by the jet temperature and therefore the jet exit velocity.

Deprés et al. [15] found broad band fluctuating pressures at higher frequencies located at the end of the nozzle

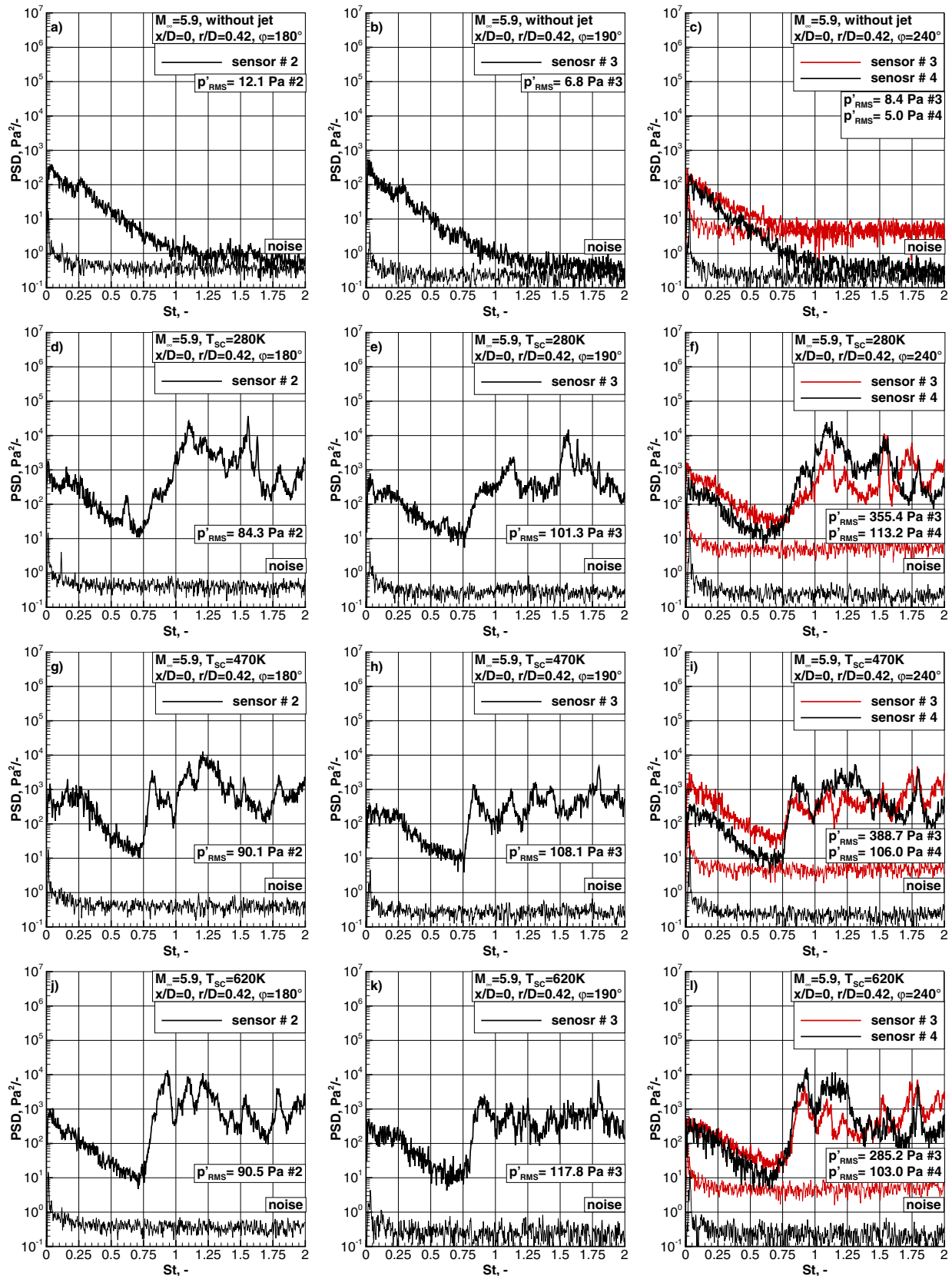
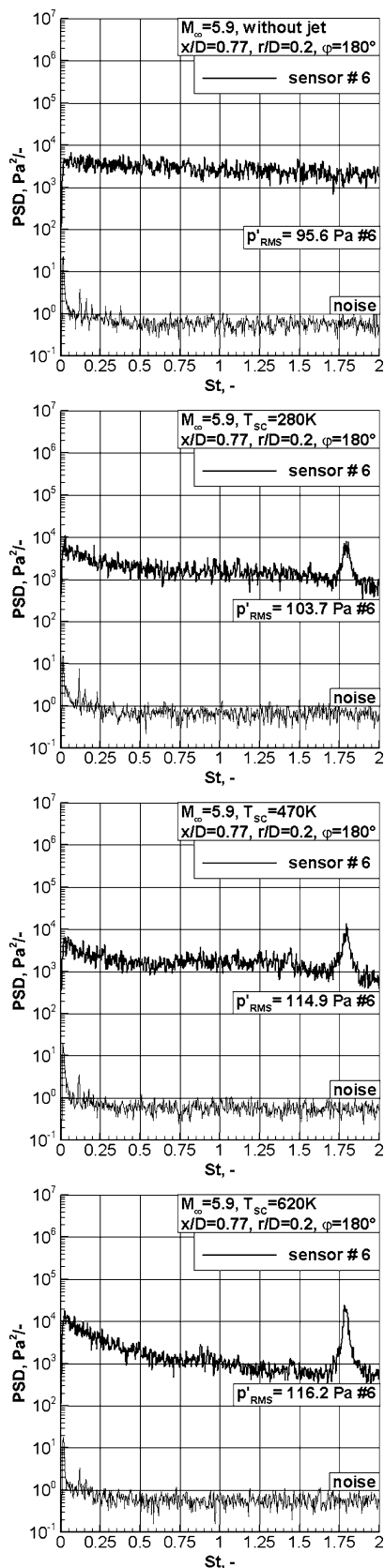


Fig. 29 PSD at  $M_\infty = 5.9$  for base sensors. Column base sensor position. Line without jet and varied jet temperatures





**Fig. 30** PSD at  $M_\infty = 5.9$  for nozzle fairing sensor. Line without jet and varied jet temperatures

fairing ( $x/D = 0.55, L/D = 0.6; x/D > 0.99, L/D = 1.2$ ). They attribute these oscillations to the interaction between the separated shear layer and the jet located downstream of the nozzle. These high-pressure fluctuations due the signature of the over-expanded jet noise generated after the nozzle exhaust are not observed in the base pressure spectra.

Statnikov et al. [26] found peaks at higher frequencies corresponding to the presence of a highly under-expanded jet. They assume that due to the larger total length of the shear layer and the enhancement of the turbulent mixing by the recirculation vortices inside the cavity results in the development of shear layer instabilities.

Figure 29 shows the base pressure spectra for the hypersonic configuration within a broad band energy above  $St > 0.75$ . These fluctuations may also show the signature of the jet noise generated due to the highly under-expanded plume. This effect occurs downstream of the nozzle fairing and is not visible in the spectra shown in Fig. 30 (sensor at  $x/D = 0.77, L/D = 1.2$ ). For the supersonic configuration these broad band fluctuations do not appear due to the much lower degree of under-expansion.

To sum up, Deprés et al. [15] found high-frequency broad band fluctuations on the nozzle fairing as signature of the over-expanded jet. Stanikov et al. [26] found high-frequency peaks on the base and nozzle wall by the presence of a highly under-expanded jet. Hence, these high-pressure fluctuations on the base and nozzle fairing can be associated to the signature of the plume. The visibility of these high-pressure fluctuations depend on reattachment of the flow. For a reattached flow (Deprés [15], supersonic configuration), the signature of the jet is not visible on the base. However, for a highly after-expanded plume (Stanikov [26], hypersonic configuration) the flow is not reattached on the nozzle fairing. Therefore, the jet noise is radiated up to the base. That implies that a highly after-expanded plume, at high altitudes, may cause high acoustical loads on a launcher base.

Research into the dynamic behavior of the shear layer is a current focus of numerical simulations in the collaborative research center TRR 40. The present results confirm the need to vary shear-layer velocities in experimental jet simulation facilities.

## 6 Summary

The design approach for an efficient jet simulation facility was presented along with first measured results. Our analysis revealed that the jet simulation for rocket after bodies depends on several similarity parameters. Important parameters are the velocity ratio to reproduce the turbulent stresses and associated mixing process and the jet flow momentum ratio to reproduce the mixing layer growth. It

appears that using the Ludwieg Tube operation principle for jet simulation opens the path to suited variations of these parameters in afterbody flow research, since the jet simulation can be efficiently performed with different gases including low molar mass gas helium. As the diameter of the jet flow storage tube is limited for given model strut sizes our present experiments show pressure losses during runtime of the jet simulation facility that are caused by the relatively large storage tube Mach number. These losses could be reduced by increasing the jet simulation storage tube in alternate jet simulations. The pitot pressure distributions of the plume flow at different axial positions are investigated and discussed. The experiments confirm the high-quality nozzle flow and plume representation of the new facility.

The topology of the mean afterbody flow field is presented by Schlieren pictures and mean pressure measurements. The large displacement effect by the under-expanded plume is evident from these results.

The analysis of the unsteady pressure in the recirculation region displays a variety of distinct frequencies with high fluctuation content. A peak compared to the well-known “shedding” at the base near  $St = 0.25$  was observed for the supersonic and hypersonic configuration. The jet always moves this peak to smaller frequencies while the fluctuation level decreases around the circumference. For the supersonic configuration the influence of the jet flow is rather limited, as only weak peaks in the spectra at high frequencies are found. For the hypersonic configuration a strong unsteady effect caused by the strong under-expanded plume is shown. This increases the fluctuation level for  $St > 0.75$ . Peaks related to longitudinal pumping, swinging and radial flapping motion of the shear layer are found, based on published numerical flow analysis. Further peaks at higher frequencies are also found. These peaks indicate a high-energy motion of the shear layer. As the variation of jet total temperature displayed a significant effect on the amplitude and Strouhal number of pressure fluctuations, it is concluded that representation of jet velocity parameters is important for representing the afterbody dynamics. Future works will further examine the afterbody flow fields by increasing the jet velocity using helium as working gas.

**Acknowledgments** The work was funded by the German Research Foundation (Deutsche Forschungsgemeinschaft, DFG) within the framework Sonderforschungsbereich Transregio 40 (Technological foundations for the design of thermally and mechanically highly loaded components of future space transporting systems). The authors thank R. Müller-Eigner (Hyperschall Technologie Goettingen GmbH, HTG, Katlenburg-Lindau) for the efforts in designing and manufacturing the jet simulation facility and D. Saile (German Aerospace Center, DLR, Cologne) and V. Statnikov (RWTH Aachen) for supporting the PSD analysis.

## References

1. Delery, J., Sirieix, M.: Base flows behind missiles. AGARD LS-98, vol. 6, pp. 1–78 (1979)
2. Shvets, A.: Base pressure fluctuations. *Fluid Dyn.* **14**(3), 394–401 (1979)
3. Eldred, K.: Base pressure fluctuations. *J. Acoust. Soc. Am.* **33**(1), 59–63 (1961)
4. Herrin, J.L., Dutton, J.C.: The turbulence structure of a reattaching axisymmetric compressible free shear layer. *Phys. Fluids* **9**, 3502 (1997). doi:[10.1063/1.869458](https://doi.org/10.1063/1.869458)
5. Mabey, D.G.: Some measurements of base pressure fluctuations at subsonic and supersonic speeds. Aeronautical Research Council, ARC-CP-1204, pp. 1–11 (1972)
6. Deck, S., Thorigny, P.: Unsteadiness of an axisymmetric separating-reattaching flow: numerical investigation. *Phys. Fluids* **19**, 065103 (2007). doi:[10.1063/1.2734996](https://doi.org/10.1063/1.2734996)
7. Janssen, J.R., Dutton, J.C.: Time-series analysis of supersonic base-pressure fluctuations. *AIAA J.* **42**(3), 605–613 (2004)
8. Herrin, J.L., Dutton, J.C.: Supersonic base flow experiments in the near wake of a cylindrical afterbody. *AIAA J.* **32**(1), 77–83 (1994)
9. Xiao, Z., Fu, S.: Studies of the unsteady supersonic base flows around three afterbodies. *Acta. Mech. Sin.* **25**, 471–479 (2009). doi:[10.1007/s10409-009-0248-4](https://doi.org/10.1007/s10409-009-0248-4)
10. Weiss, P.-E., Deck, S., Robinet, J.-C., Sagaut, P.: On the dynamics of axisymmetric turbulent separating/reattaching flows. *Phys. Fluids* **21**, 075103 (2009). doi:[10.1063/1.3177352](https://doi.org/10.1063/1.3177352)
11. Bitter, M., Scharnowski, S., Hain, R., Kaehler, C.J.: High-repetition-rate PIV investigations on a generic rocket model in sub- and supersonic flows. *Exp. Fluids* **50**, 1019–1030 (2011). doi:[10.1007/s00348-010-0988-8](https://doi.org/10.1007/s00348-010-0988-8)
12. Simon, F., Deck, S., Guillen, P., Sagaut, P.: Reynolds-averaged navier–stokes/large-eddy simulations of supersonic base flow. *AIAA J.* **44**(11), 2578–2590 (2006)
13. Sahu, J.: Computations of supersonic flow over a missile afterbody containing an exhaust jet. *J. Spacecr.* **24**(5), 403–410 (1987)
14. Kawai, S., Fujii, K.: Computational study of supersonic base flow using hybrid turbulence methodology. *AIAA J.* **43**(6), 1265–1275 (2005)
15. Deprés, D., Reijasse, P.: Analysis of unsteadiness in afterbody transonic flows. *AIAA J.* **42**(12), 2541–2550 (2004)
16. Sahu, J., Heavey, K.R.: Numerical investigation of supersonic base flow with base blees. *J. Spacecr. Rocket.* **34**(1), 61–69 (1995)
17. Wong, H., Meijer, J., Schwane, R.: Theoretical and experimental investigations on Ariane 5 base-flow buffeting. In: Proceedings of the 5th European Symposium on Aerothermodynamics for Space Vehicles, ESA Publications Division ESTEC, Noordwijk, The Netherlands (ESA SP-563) (2005)
18. Bergman, D.: Effects of engine exhaust flow on boattail drag. *J. Aircr.* **8**(6), 434–438 (1971)
19. Weiss, P.E., Deck, S., Sagaut, P.: Zonal-detached-eddy-simulation of a two-dimensional and axisymmetric separating/reattaching flow. In: 38th Fluid Dynamics Conference and Exhibit, Seattle, Washington, AIAA 2008-4377, 23–26 June 2008
20. Venkatakrisnan, L., Suriyanarayanan, P., Mathur, N.B.: BOS density measurements in afterbody flows with shock and jet effects. In: 37th AIAA Fluid Dynamics Conference and Exhibit, Miami, FL, AIAA 2007-4223, 25–28 June 2007
21. Peters, W.L., Kennedy, T.L.: Jet simulation techniques—simulation of aerodynamic effects of jet temperature by altering gas compositions. In: Proceedings of the 17th Aerospace Sciences Meetings, American Institute of Aeronautics and Astronautics (1979)

22. Peters, W.L., Kennedy, T.L.: An evaluation of jet simulation parameters for nozzle/afterbody testing at transonic mach number. In: Proceedings of the 15th Aerospace Sciences Meetings, American Institute of Aeronautics and Astronautics (1977)
23. Kumar, R., Viswanah, P.R.: Mean and fluctuating pressure in boat-tail separated flows at transonic speeds. *J. Spacecr. Rocket.* **39**(3), 430–438 (2002)
24. Reijasse, P., Delery, J.: Experimental analysis of the flow past the afterbody of the Ariane 5 European launcher. *J. Spacecr. Rocket.* **31**(2), 208–214 (1994). doi:[10.2514/3.26424](https://doi.org/10.2514/3.26424)
25. Statnikov, V., Saile, D., Meiß, J.H., Henckels, A., Meinke, M., Guelhan, A., Schroeder, W.: Experimental and numerical investigation of the turbulent wake flow of a generic space launcher configuration. In: Proceedings of the 5th European Conference for Aerospace Sciences, EUCASS (2013)
26. Statnikov, V., Sayadi, T., Meinke, M., Schmid, P., Schröder, W.: Analysis of pressure perturbation sources on a generic space launcher afterbody in supersonic flow using zonal turbulence modeling and dynamic mode decomposition. *Phys. Fluids* **27**(1) (2015). doi:[10.1063/1.4906219](https://doi.org/10.1063/1.4906219)
27. Saile, D., Guelhan, A., Henckels, A., Glatzer, C., Statnikov, V., Meinke, M.: Investigations on the turbulent wake of a generic space launcher geometry in the hypersonic flow regime. *EUCASS Prog. Flight Phys.* **5**, 209–234 (2013). doi:[10.1051/eucass/201305209](https://doi.org/10.1051/eucass/201305209)
28. Saile, D., Guelhan, A.: Plume-induced effects on the near-wake region of a generic space launcher geometry. In: Proceedings of the 32nd AIAA Applied Aerodynamics Conference, AIAA 2014–3137 (2014)
29. Koppenwallner, G., Mueller-Eigner, R., Friehmelt, H.: HHK Hochschul-Hyperschall-Kanal: Ein “Low cost” Windkanal für Forschung und Ausbildung. *DGLR Jahrbuch, Band 2*, 887–896 (1993)
30. Pindzola, M.: Jet simulation in ground test facilities. *AGARDograph* **79**(11), 1–56 (1963)
31. Hannemann, K., Luedeke, H., Pallegoix, J.F., Ollivier, A., Lambare, H., Maseland, J.E.J., Geurts, E.G.M., Frey, M., Deck, S., Schrijer, F.F.J., Scarano, F., Schwane, R.: Launch vehicle base buffeting—Recent experimental and numerical investigations. In: Proceedings of 7th European Symposium on Aerothermodynamics, ESA Communications ESTEC, Noordwijk, The Netherlands (ESA SP-692) (2011)
32. Estorf, M., Wolf, T., Radespiel, R.: Experimental and numerical investigations on the operation of the hypersonic Ludwig tube Braunschweig. In: Proceedings of the 5th European Symposium on Aerothermodynamics for Space Vehicles, ESA SP-563, 579–586 (2005)
33. Wu, J., Radespiel, R.: Tandem nozzle supersonic wind tunnel design. *Int. J. Eng. Syst. Model. Simul. Proc.* **5**(1), 8–18 (2013). doi:[10.1504/IJESMS.2013.052369](https://doi.org/10.1504/IJESMS.2013.052369)
34. Wu, J., Radespiel, R., Zamre, P.: Disturbance characterization and flow quality improvement in a Tandem Nozzle Mach 3 Wind Tunnel. *Exp. Fluids* (2015). doi:[10.1007/s00348-014-1887-1](https://doi.org/10.1007/s00348-014-1887-1)
35. Saile, D., Henckels, A., Guelhan, A.: Design of the TIC-nozzle and Definition of the Instrumentation. In: ADAMS, N.A. et al. (eds) DFG Sonderforschungsbereich/Transregio 40—Annual Report 2009, TU München, Garching (2009)
36. Gruemmer, K.: Ein Rechenprogramm für den Entwurf ebener und rotationsymmetrischer Überschallwindkanaldüsen. *DFVLR-FB 76–59*, Deutsches Zentrum für Luft, Und Raumfahrt, Cologne (1976)
37. Launch Kit Flight 202 Ariane 5. <http://www.astrium.eads.net/en/launch-kits/launch-kit-flight-202-ariane-5-st2-gsat-8-insat-4g.html> (2013). Accessed 11 March 2013
38. Ali, S.R.C., Wu, J., Radespiel, R., Schilden, T., Schroeder, W.: High-frequency measurements of acoustic and entropy disturbances in a hypersonic wind tunnel. In: Proceedings of the 44th AIAA Fluid Dynamics Conference (2014). doi:[10.2514/6.2014-2644](https://doi.org/10.2514/6.2014-2644)
39. Morkovin, M.V.: Fluctuations and hot-wire anemometry in compressible flows. *AGARD-AG-24* (1956)
40. Kovasznay, L.S.: Turbulence in supersonic flow. *J. Aeronaut. Sci.* **20**, 657–674 (1953)
41. Laufer, J.: Some statistical properties of the pressure field radiated by a turbulent boundary layer. *Phys. Fluids* (1958–1988) **7**(8), 1191–1197 (1964)
42. Stainback, P.C., Wagner, R.D.: A comparison of disturbance levels measured in hypersonic tunnels using a hot-wire anemometer and a pitot pressure probe. In: Proceedings of the 7th Aerodynamic Testing Conference. AIAA paper no. 72–1003. Palo Alto, California, Sep. 13–15 (1972)
43. Pain, R., Weiss, P.E., Deck S.: Zonal detached eddy simulation of the flow around a simplified launcher afterbody. *AIAA J.* **52**(9), 1967–1979 (2014). doi:[10.2514/1.J052743](https://doi.org/10.2514/1.J052743)
44. Schwane, R.: Numerical prediction and experimental validation of unsteady loads on Ariane 5 and VEGA. *J. Spacecr. Rocket.* **52**(1), 54–62 (2015). doi:[10.2514/1.A32793](https://doi.org/10.2514/1.A32793)